Synthetic Aperture Ladar for High-Resolution Ground-Based Imaging of Objects in LEO, GEO, and Cis-Lunar Space

THOMAS J. KARR, Life Member, IEEE
MITRE Corporation, McLean, VA USA

Space domain awareness of geosynchronous altitude, and beyond to cis-Lunar and deep space, requires that we detect, track, and *characterize* all objects that may present a threat to critical national and commercial space and Earth-bound assets. Characterization of a space object includes understanding its potential capabilities. Imaging a space object with a resolution of a few centimeters can reveal the object's apertures, antennae, thrusters, secondary payloads, and other attributes, thereby contributing a great deal to characterizing the object. Passive optical imaging at GEO and cis-Lunar range, at centimeter resolution, requires an unfeasibly large ∼1000 m real aperture, and long-baseline optical interferometry requires many separate apertures over many comparably large baselines combined and phased for measurements of a broad range of spatial frequencies. Synthetic aperture laser imaging with a single aperture can achieve centimeter resolution at a long range far below the real aperture diffraction limit, if the active sensor has sufficient coherence and power-aperture. We discuss how an active laser radar could collect centimeter-class imagery, we analyze the principal constraints such a sensor must meet, and we estimate the power and aperture needed to image at GEO and cis-Lunar distances. We conclude that current and anticipated HEL sources with power of tens to hundreds of kilowatts transmitted and received through existing large ground-based telescopes have sufficient coherence and power and aperture, and current optics, electronics, and signal processing have sufficient capability to enable centimeter-class imaging to cis-Lunar space and submeter class imaging of the Lunar surface.

Manuscript received 13 October 2023; revised 11 April 2024; accepted 19 April 2024. Date of publication 3 May 2024; date of current version 9 August 2024.

DOI. No. 10.1109/TAES.2024.3396417

Refereeing of this contribution was handled by K. Peter Judd.

Author's address: Thomas J. Karr is with MITRE Corporation, McLean, VA 22102-7539 USA, E-mail: (tkarr@mitre.org).

NOMENCLATURE

LEO	Low Earth orbit.
MEO	Medium Earth orbit.
GEO	Geosynchronous Earth orbit.
HEO	Highly elliptical Earth orbit.
NTM	National technical means.
IR	Infrared.
EO	Electro–optical.
PSD	Power spectral density.
LO	Local oscillator.
CNR	Clutter-to-noise ratio (additive noise).
SNR	Signal-to-noise ratio.
PSLR	Peak sidelobe ratio.
cr	Coherent-on-receive cancellation ratio.
IPR	Impulse response.
SDA	Space domain awareness.
P_{avg}	Average transmitted power at the transmitter aperture.
P_{pk}	Peak transmitted power at the transmitter aperture $= P_{\mathrm{avg}}/f_d$.
M	Design power margin.
$\mathrm{L_{ant\_t}}$	Signal transmission fraction in transmitter antenna.
$\mathrm{G_{ctr\_r}}$	Receiver on-axis gain fraction due to all nonideal beam features.
$\mathrm{D_T}$	Transmitter aperture diameter.
$\mathrm{A_T}$	Transmitter aperture area.
$\mathrm{G_T}$	Transmitter aperture gain.
λ	Wavelength.
ρ_{r}	Range IPR.
κ_{r}	Full bandwidth correction for range IPR.
R	Range from sensor to target satellite.
$\hat{\boldsymbol{n}}$	Unit vector normal to the SAL slant plane.
$\mathrm{R_\oplus}$	Earth equatorial semimajor axis.
$\mathrm{V_{sat}}$	Target satellite speed.
ω	Target rotation rate with respect to sensor.
L	Synthetic aperture length.
$\mathrm{f_d}$	Duty factor $= \tau\ \mathrm{f_{pulse.}}$
σ_0	Target backscatter fraction.
θ_{i}	Incident angle on target.
θ_{g}	Grazing angle on target.
η	Twist angle.
$\mathrm{L_C}$	Fraction of coherent signal remaining after all transmitter, propagation, receiver, and processing losses.
$\mathrm{L_{aspect}}$	Signal fraction due to antenna aspect with respect to target.
$\mathrm{L_{trans}}$	Fraction of signal passing through transmitter optics.
$\mathrm{L_{misc}}$	Fraction of signal (equivalent noise increase) passing through miscellaneous errors.
$\mathrm{T_{rcv}}$	Receiver noise temperature.
$\mathrm{Q_e}$	Detector quantum efficiency.
η_{het}	Heterodyne efficiency.
$\mathrm{r_0}$	Atmospheric turbulence coherence length.
$\mathrm{V_{wind}}$	Wind speed.
h	Planck constant.

LOS	Line of sight.
RF	Radio frequency.
PHD	Phase history data.
SAR	Synthetic aperture radar.
ISAR	Inverse synthetic aperture radar.
SAL	Synthetic aperture laser radar.
ISAL	Inverse synthetic aperture laser radar.
I/Q	In phase and quadrature.
SOLO	Stable optical local oscillator.
MNR	Multiplicative noise ratio.
ANR	Additive noise ratio.
ISLR	Integrated sidelobe ratio.
U(f)	Power spectral density (SOLO or PHD).
IPP	Interpulse period.
f_{pulse}	Pulse repetition rate = 1/IPP.
T_{RT}	Round-trip time.
S_T	Transmitter Strehl ratio.
Ψ_T	Transmitted beam divergence.
S_R	Receiver Strehl ratio.
L_{ant_r}	Signal transmission fraction in receiver antenna.
G_{ctr_t}	Transmitter on-axis gain fraction due to all non-ideal beam features.
D_R	Receiver aperture diameter.
A_R	Receiver aperture area.
G_R	Receiver aperture gain.
B	Waveform bandwidth.
ρ_{az}	Azimuth IPR.
κ_a	Full filter correction for azimuth IPR.
R_s	Semimajor axis of target orbit.
$\hat{\boldsymbol{q}}$	Unit vector parallel to orb angular momentum.
τ	Pulse duration.
V_{obs}	Observer (SAL) speed.
V	Target speed relative to sensor = ωR.
T_{ap}	Synthetic aperture time = $T_{coh.}$
CPP	Coherent processing period $\geq T_{ap.}$
ρ	Target equivalent Lambertian reflectivity.
φ	Doppler cone angle; 90° = broadside.
ψ_0	Slope angle.
ψ	Squint angle.
L_{rcv}	Fraction of signal passing through receiver optics.
L_{atm}	Fraction of signal passing through atmospheric path.
L_{corner}	Fraction of signal (equivalent noise increase) passing to/from image corners and edges.
L_{proc}	Fraction of signal passing through processing.
F	Receiver noise figure.
η_d	Detection efficiency.
k	Boltzmann constant.
l_0	Atmospheric turbulence outer scale.
SNR	Signal-to-noise ratio with speckle.
c	Speed of light.

I. INTRODUCTION

The U.S. and its allies and partners have critical national security and commercial assets in space at all altitudes: LEO (remote sensing, communication, weather, NTM, SDA), MEO (navigation), and HEO/GEO (communication, missile warning, weather, NTM, SDA). We anticipate the U.S. soon will place many critical assets into orbits beyond GEO, including into cis-Lunar space and around the Moon [1]. Valuable assets must be protected from threats, both natural and man-made. Consequently, we anticipate there will be an urgent need to catalog, track, and *characterize* all the objects in space between the Earth and the Moon (and eventually beyond the Moon).

Characterization of a resident space object includes assessing its capabilities, which include estimating its capacity of maneuvering, understanding what sensors it carries, understanding what communication channels it may use to send data to Earth or other space platforms, knowing whether and how many deployable "daughter" satellites it carries, and assessing the capabilities of the "daughters." High-resolution imagery of the target satellite may contribute critical information for characterization.

Ground-based assets exist to track and characterize many LEO objects, thereby determining their capabilities and threat potential. The assets include the Space Fence radar [2], various other radars for space object identification [3], passive optical imaging with and without adaptive optics [3], and ground-based inverse synthetic aperture radar (ISARs) for high-resolution imaging [4]. Objects at higher altitudes (MEO, GEO, and HEO) can be detected and tracked from the Earth optically and by radar [3], and much can be learned from the satellites' multi- and hyperspectral EO, IR and RF signatures. But Earth-based imagery does not presently contribute a great deal to *characterization* of satellites at those high altitudes.

A high-resolution centimeter-class image of a satellite would greatly contribute to our full characterization of it [5]. However, how to collect such images? Passive high-resolution imaging of deep space objects presents many challenges. A high-resolution image of a high-altitude or deep-space object of interest could be collected with a close fly-by of an inspector satellite. But high-altitude space is so vast—trillions of cubic kilometers out to GEO, and three orders of magnitude larger out to the Earth-Moon L1 point—that close fly-by imaging and characterization probably is not practicable for all the objects that could be out there. Ground-based real-aperture passive optical imaging of GEO at centimeter-class resolution would require an aperture of ∼1000 m. Sparse multiaperture arrays of telescopes made of many "small" apertures spread out over hundreds of meters of ground and coherently combined in an optical interferometer have been used by astronomers to obtain high-resolution information on extrasolar objects [6], sparse and filled arrays have been proposed and studied as possible characterization sensors of high-altitude satellites [44], [48], and optical interferometric fringes have been observed from high-altitude satellites with the navy prototype optical interferometer [7], [46], [47]. Passive phased arrays large enough for high-resolution imaging of high-altitude satellites are theoretically possible but, with their many unsolved technical challenges, a ground-based passive phased-array facility sufficient for centimeter-class

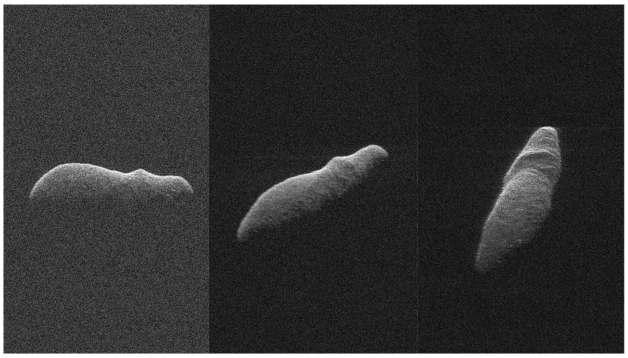

Fig. 1. Radar image of Asteroid SD220 at 1.8 million miles, collected by bistatic SAR in 2019 transmitting from NASA's 70 m communications complex in California and receiving at NSF's 100 m Green Bank Telescope in West Virginia [10]. IPR is ∼12 ft.

imaging of satellites in GEO and higher altitude would be a very large engineering project, and no such facility for passive centimeter-class imaging has advanced beyond the early concept stage [45].

There is another way to get high-resolution images at long range: synthetic aperture radar (SAR) imaging. SAR uses the relative motion between the sensor and the target object to form a "synthetic" pupil much larger than the real antenna size, collects "phase history data (PHD)" over this synthetic aperture, and then uses analog or digital signal processing to create an image from the PHD [4]. In principle, a SAR can achieve any desired resolution at any range, if certain physics constraints are met. Chief among these constraints is that 1) coherence must be maintained or reconstructed over the entire synthetic aperture, and 2) the radar power and aperture must be sufficient for the signal to dominate over noise. SAR is a mature technology, and ISAR has been used for many years to collect high-resolution radar images of LEO objects and low-resolution images of deep space objects [8], [9] (see Fig. 1).

However, high-resolution ISAR using electromagnetic radiation at radio frequencies (RF) is limited to characterizing only LEO satellites. Also, the latest generation of cubesats has features so small that they cannot be completely characterized by ISAR.

Synthetic aperture laser radar or ladar (SAL), with its higher frequency and shorter wavelength than RF radar, can overcome ISAR's limitations and could, in principle, image space objects at centimeter-class resolution in GEO and beyond in deep space. The objectives of this article are to estimate the requirements for a deep space satellite-characterizing centimeter-class inverse synthetic aperture laser radar (ISAL), and to show that such an ISAL is feasible with the currently available technology of laser sources, detectors, optics, telescopes, and processing.

This article applies the SAR theory of space imaging to SAL and ISAL imaging.

The rest of the article is organized as follows. In Section II, we show how SAR and SAL work, and we introduce the physics constraints on SAR and SAL. In Section III, we discuss the energy-aperture theorem and the scaling relations of power, aperture, range, wavelength, etc., for SAR and SAL. In Section IV, we introduce the various noise sources and image quality metrics that must be considered in collecting SAR or SAL images. In Section V, we show that natural satellite motion in GEO and beyond is sufficient to collect centimeter-class images with an ISAL sensor. We also discuss the image effects of more complex target motions. In Section VI, we discuss the coherence requirements on an ISAL for high-resolution imaging, including the effects of laser source noise and atmospheric turbulence. In Section VII, we estimate the laser source power needed to collect centimeter-class ISAL images in LEO, GEO, and cis-Lunar-to-Lunar deep space. We will see that HEL power levels—from tens of kilowatts up to a few megawatts—are needed depending on target range and the desired resolution. In Section VIII, we discuss some ISAL system features of deep space imaging. Our summarizing discussion is in Section IX.

II. SYNTHETIC APERTURE RADAR AND LADAR IMAGING

SAR builds an image from the reflection of successive radar pulses transmitted at a target. Although a passive optical image is a two-dimensional image of elevation-azimuth cells or pixels, the SAR image is a two-dimensional image of range-azimuth cells or pixels. Moreover, where passive optical images are described by their "resolution," radar images are described by their "impulse response" or IPR, that is, the response in range and azimuth to imaging a point target. The range dimension information comes from the time-of-flight of the radar pulse, or equivalently from the bandwidth of the radar signal. The azimuth information comes from the successive lines of sight to the target—each radar pulse is transmitted/received on a unique LOS, and the LOS subtend an angle at the target. Each received radar pulse is measured as I/Q data and stored as a complex number with amplitude and phase. The image is constructed by coherently combining the data from all the pulses [11]. The process is shown schematically in Fig. 2.

The collection of pulse-by-pulse SAR measurements is called the PHD. The PHD is a time and space sampling of the RF field (amplitude and phase) over the 1-D azimuth pupil spanned by all the locations of the real receiving aperture relative to the target object, as illustrated in Fig. 3. The 1-D range image at each point in the azimuth pupil is the Fourier transform of the RF spectrum of the pulse. By Galilean invariance, the same information is collected whether the receiver moves past a stationary target—called SAR—or the target rotates in front of a stationary receiver—called inverse SAR or ISAR. Applying the Van Cittert-Zernike theorem [12], the range-resolved azimuth image of the target is the Fourier transform of the field in the pupil at each range [13]. Note that all the PHD are collected in a single coherent spot of the SAR beam. The transmitting antenna should be coherent to maximize the power in this spot on the target. The receiving antenna must be coherent to measure the round-trip phase shift of the reflected beam.

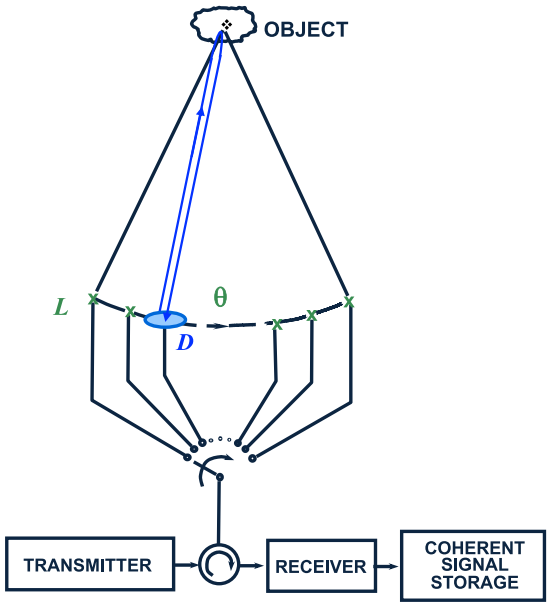

Fig. 2. With a real aperture D, the round-trip signal is I/Q sampled at each relative azimuth location across the large aperture L (the pupil plane) or over angle θ, either by aperture motion or object rotation. This PHD from the synthetic pupil is coherently combined into a complex-number image.

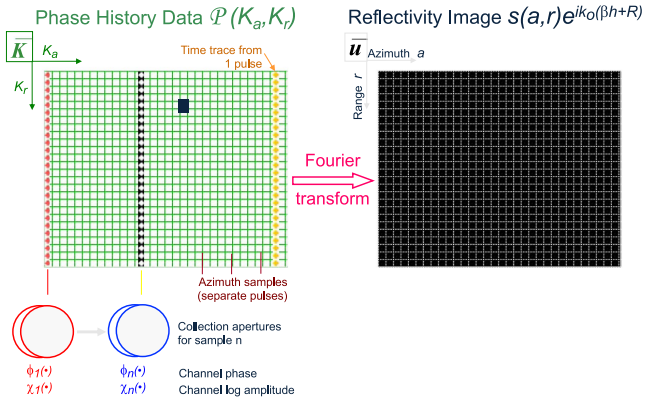

Fig. 3. PHD and the complex number "image" formed from it. The PHD is a 2-D time-space I/Q sampling of the field in the pupil of the sensor.

The SAR data may be presented as an intensity image, but it is created as a complex-number amplitude and phase image. As such, it contains much more information than an intensity-only passive EO/IR image.

The value of SAL/ISAL imaging is that it can achieve an arbitrarily high image "resolution," that is, *arbitrarily small IPR*, at *any* range to target, *if certain conditions are met*. IPR is usually described in terms of its width at half-max or "3 dB width." The range IPR 3 dB width is [13]

$$\rho_r = \frac{\kappa_r c}{2B} \tag{1}$$

and the azimuth IPR 3 dB width is [13]

$$\rho_{az} = \frac{\kappa_a \lambda}{2\theta} = \frac{\kappa_a \lambda R}{2VT_{ap}}. \tag{2}$$

Since the "image" of a point scatterer is the result of digital filtering, a point image has sidelobes (the radar equivalent of Airy rings on the optical point spread function). The κ_r and κ_a are tapering factors corresponding to the filters that are used to process the range and azimuth data and control the height of sidelobes.

Two conditions must be met to create a SAR/ISAR image. 1) Since each sample in the pupil plane measures the amplitude and accumulated round-trip phase of each pulse, the phase measurement must be coherent (i.e., have very small random pulse-to-pulse noise) over the entire PHD. In principle, coherence can be enforced in postprocessing the PHD, but SAR image processing is simplified if the LO is coherent over the entire PHD and only non-LO phase noise must be corrected in processing. Large random phase errors from pulse to pulse due to, e.g., a wildly unstable local oscillator (which is no phase reference at all) make the recovery of coherence in processing difficult. If, however, the LO is sufficiently coherent over each single pulse and the phase changes relatively slowly from pulse-to-pulse during the PHD, then an image can be recovered in processing. We have more detail on coherence in Section VI and processing in Section VIII. 2) The transmitter and receiver must have sufficient power and aperture to have energy greater than noise in each image range-azimuth cell after all collection and processing. We have more details about this requirement in Section III.

If the LO phase drifts over the PHD synthetic aperture time $T_{\rm ap}$ but is sufficiently stable over each pulse, then overall coherence of the PHD can be recovered by using the LO to measure the phase of each transmitted pulse and its received reflection; the phase *change* over the pulse round trip is the information needed to form the azimuth image. The radar world calls this approach "coherent on receive" [14]; it was common in the early decades of SAR when the RF LO was not stable over $T_{\rm ap}$.

A SAL works the same way as a SAR. A SAL schematic is shown in Fig. 4. The significant differences between SAR and SAL are as follows.

1) A SAR has an LO stable over the entire synthetic aperture. A SAL has an optical LO which may be stable over only a single pulse round-trip, and the entire SAL PHD may be made "coherent on receive."
2) A SAR has antennas. A SAL has a beam director and a receiving telescope, which may be the same optic (monostatic system) or two different optics (bistatic system).
3) A SAR receiver electronically mixes the received signal and LO. A SAL receiver is an optical heterodyne detector where the optical LO is spatially interfered with the received signal and the beat wave measured.
4) SAR dominant receiver noise is thermal. SAL dominant receiver noise is quantum heterodyne noise.
5) A SAR is sensitive to its receive antenna angular pattern. A SAL is sensitive to its heterodyne detection angular pattern.

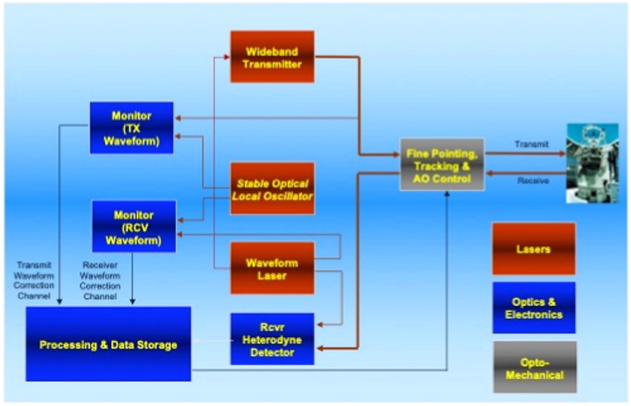

Fig. 4. Notional SAL with SOLO, low-power waveform-generating laser, wideband transmitter source, heterodyne signal detector, and coherent detection of the transmitted pulses and received waveforms. A waveform laser would be mixed with the received signal for "stretch" processing of chirped waveforms [20]. The SOLO may be mixed directly with the received signal without stretch processing.

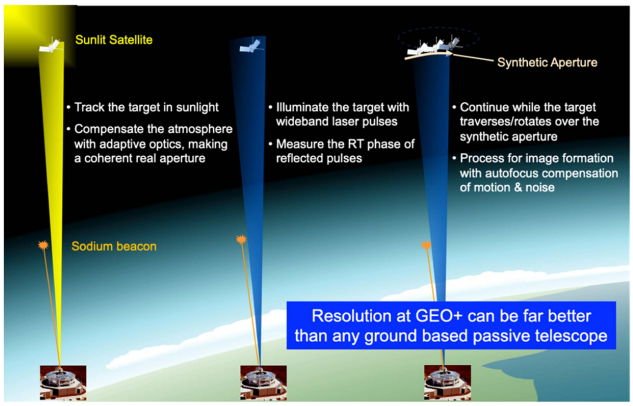

Fig. 5. Notional ISAL imaging a satellite.

6) A SAL is sensitive to atmospheric turbulence in the real transmit and receive apertures, creating several sources of noise unique to SAL.

Synthetic aperture ladar was first demonstrated in a laboratory setting in one dimension in 1995 [15], and in two dimensions in 2002 [16] and 2005 [17]. SAL was first demonstrated from airborne platforms in DARPA's *Synthetic Aperture Ladar for Tactical Imaging* program in 2006 [18], [19].

A ground-based ISAL must use a laser operating at a wavelength transmissible through the atmosphere to space. Lasers exist for several atmospheric windows with low absorption and scattering loss: long-wave infrared (8–12 μm), midwave infrared (3.5–4.2 μm), short-wave infrared (various windows in 1.2–2.2 μm), and the visible and near-infrared (0.4–1.2 μm) [52].

An ISAL could collect PHD to image satellites by using the natural rotation of those satellites with respect to a point on the Earth. The approach is illustrated in Fig. 5. The target satellite should be sunlit so that the telescope tracking system can see it and point the SAL laser to illuminate and dwell on the moving target. The sunlit target satellite is tracked, and atmospheric turbulence is corrected with the help of an artificial beacon guide star. The target is illuminated with wideband laser pulses of the desired range IPR. The transmitter/receiver measures the round-trip phase shift of each pulse. The target appears to rotate with respect to the ground, creating a synthetic aperture. The tracking and illumination of the target continue over the synthetic aperture for the desired azimuth IPR. There are several possible modes of SAL/SAR collection. "Spotlight" mode collects with the SAL beam staring at the target and covering it over time $T_{\rm ap}$. "Scan" mode collects by sweeping the SAL beam across the target, with each point spending time $T_{\rm ap}$ in the beam. The modes have slightly different noise sources and magnitudes.

In Section V, we show that the Keplerian orbital satellite rotation is sufficient for ISAL imaging with centimeter-class IPR in tens of seconds or less.

The first serious development of ISAL imaging of satellites in general and GEOsats in particular, the concept in Fig. 5, was made by Northrop Grumman in DARPA's *LongView* program [21] of 2006–2008.

III. ENERGY-APERTURE THEOREM AND SYSTEM TRADES

Noise limits the resolution of every imaging system. Indeed, if optical detection was noise-free, then even a passive imaging system could achieve arbitrarily sharp resolution simply by deconvolving the image with the point-spread function measured to arbitrarily high dynamic range and spatial frequency [22].

We can calculate the average ratio of the signal energy in a target point scatterer image to additive noise (noise the receiver adds independent of the point scatterer's signal) in the absence of speckle or other fluctuations. Traditionally, the target's image is denoted as "clutter," and this ratio is denoted as "clutter-to-noise ratio" or CNR. Note that signal-to-noise ratio (SNR) includes speckle and other fluctuations; a single SAR image capture has SNR = 1, even though the CNR may be very large. Speckle makes a point scatter's energy fluctuate over a very large range of values; in a single image capture with speckle, the average energy of point scatterers distributed evenly over the image area would be the CNR.

The SAR energy-aperture theorem sets a lower bound for the total source energy required in the coherent integration time, or equivalently on the average power of the source, to achieve range IPR ρ_r at CNR. The required average power can be calculated from the standard radar equation using the Van Cittert–Zernike theorem to transform PDH into the image. The result for the average source power is [23], [24]

$$P_{\rm avg} = \frac{2(4\pi)^3\, R^4\, \omega\, F\ [\text{additive noise}]\ M\ \text{CNR}\ \sin\varphi\ \cos\psi_0}{\kappa_a\, \rho_r\, \lambda^3\, G_T\, G_R\, \eta_d\, L_C\, (\text{LOS})\ \sigma_0\left(\theta_g\right)}. \tag{3}$$

More noise means more power (for constant CNR) or a larger range IPR (for constant power).

The transmit and antenna gains G_T and G_R in (3) include on-axis losses inside the antennae and the antennae Strehl ratios but all off-axis effects are in the loss L_C. Any desired azimuth IPR can be achieved simply by collecting pulses with average power P_{avg} over the required aperture time T_{ap} or equivalently the required angle ωT_{ap}. The peak power required from the source with duty factor f_d is

$$P_{pk} = P_{\text{avg}}/f_d \ . \tag{4}$$

In (3), σ_0 is the backscattered fraction of power or energy in a range-azimuth cell *relative to isotropic scattering into* 4π, [this is the usual radar definition of backscattering fraction, not the usual EO definition of "optical cross section"], and it is parametrized by the grazing angle on the target surface. This radar concept is more useful for SAL analysis than the concept of a target's "optical cross section" because it allows us to make the backscattering signal a function of position on the satellite's surfaces and to make direct comparisons to and use of common SAR formulae [11], [13]. "Additive noise" means the noise independent of the signal strength per unit of frequency in a single pulse measurement; for an RF radar, it is thermal noise kT_{rcv}, while for a coherent optical receiver [25], it is hc/λ. Also, the noise bandwidth is implicitly in (3) inside ρ_r, and the azimuth IPR is implicitly in (3) through the rotation rate ω. Equation (3) has a simplified power-aperture-IPR scaling for $D_T = D_R = D$

$$P \propto \frac{\lambda\,[\text{additive noise}]\,R^4\omega}{D^4\rho_r} \tag{5}$$

$$P \propto \frac{\lambda T R^4\omega}{D^4\rho_r} \quad [\text{RF}] \tag{6a}$$

$$P \propto \frac{R^4\omega}{D^4\rho_r} \quad \big[\text{optical}\big]. \tag{6b}$$

Note that the required power-aperture of a synthetic aperture ladar SAL or ISAL does not explicitly depend on wavelength; it does implicitly depend on wavelength through the backscattering ratio σ_0 and through path losses L_C.

Power required for achieving the desired IPR at the desired range depends critically on the total loss L_C(LOS), which in turn depends on the line-of-sight to each point on the target. In Section VII, we will use the "radar standard" in estimating L_C—we will estimate L_C at the LOS with the highest loss and lowest overall signal throughput so that every point in the image will equal or exceed the desired CNR.

Equation (6) shows why the ISAL needs adaptive optics in both the transmitter and receiver real apertures. Without adaptive optics in the real aperture, the coherent signal energy would be equivalent to using a real aperture the size of a single atmospheric coherence length, which is ~10–20 cm in the VNIR spectral band [49]. Since required power scales as (coherent aperture)$^{-4}$, an ISAL needs to maximize the coherent aperture size to something $>> r_0$. The transmitter needs $D_T >> r_0$ to maximize flux on the distant target. The receiver needs $D_R >> r_0$ to maximize the signal at the detector, and the receiver must be spatially coherent over D_R to measure the optical phase. Coherence over $D >> r_0$ requires adaptive optics to remove nearly all the high-spatial-frequency phase variations of atmospheric turbulence. Also, if $r_0 < D < L$, then adaptive optics over the real aperture D does not remove all phase errors across the synthetic aperture L, and compensation of this residual phase error must be done in PHD processing [26]. Sections V and VIII have more discussion on this point.

IV. IMAGE QUALITY AND NOISE SOURCES

SAR and SAL image quality metrics are somewhat different than optical image quality metrics. SAR/SAL image quality is measured by the additive noise ratio CNR (a measure of additive noise that is the same in every range-azimuth cell), the multiplicative noise ratio (MNR) (a measure of noise multiplied by the signal in a range-azimuth cell), the 3 dB range and azimuth IPR widths, the first sidelobe ratio in range and azimuth, the third sidelobe ratio, the integrated energy in all sidelobes beyond the third [denoted as integrated sidelobe ratio (ISLR)], the amount of range and azimuth aliasing after processing, and some other metrics. The most important are the CNR, 3 dB widths, and first sidelobe ratios, but all the other metrics should be estimated in the SAL/SAR design process.

SAR and SAL are sensitive to many noise sources. The additive noise ratio CNR quantifies the magnitude of noise in the receiver. In general, one can express the signal-independent additive noise power per unit of frequency as

$$\text{Additive Noise} \ = \ \begin{Bmatrix} kT_{\text{rcv}} \\ hc/\lambda \end{Bmatrix}, \tag{7}$$

where the two terms in (7) correspond to SAR and SAL. RF SAR has additive thermal noise kT_{rcv} per unit of frequency in the RF receiver. Optical SAL has additive quantum heterodyne noise hc/λ (one photon per unit of frequency) in the coherent optical detection process [24]. The total additive noise is (7) multiplied by pulse bandwidth B. All receivers have a noise figure $F > 1$ quantifying how much additive noise increases as it moves through the receiver.

All SALs and SARs have local oscillator noise. LO noise has negligible contribution to the CNR in (3), but LO phase noise degrades image quality by increasing the IPR and increasing the range and azimuth sidelobes above what the ideal compression filters create. We quantify the relationship between LO phase noise and image sidelobes in Section VI.

The PHD is a time and space sampling of the electromagnetic field in the synthetic aperture at temporal frequency $f_{\text{pulse}} = 1/\text{IPP}$ and spatial frequency $f_{\text{pulse}}/V = 1/(R\,\omega\,\text{IPP})$. Sampling inherently aliases information at higher frequencies into the sampled frequencies. Azimuth aliasing is unavoidable if the pulse frequency is too low, that is

$$f_{\text{pulse}} < \frac{2\omega R}{D}. \tag{8}$$

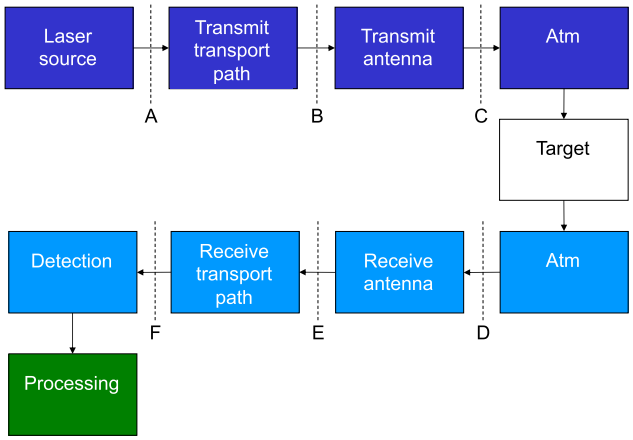

Fig. 6. Signal power path for a SAL or SAR, with losses in each step of the path.

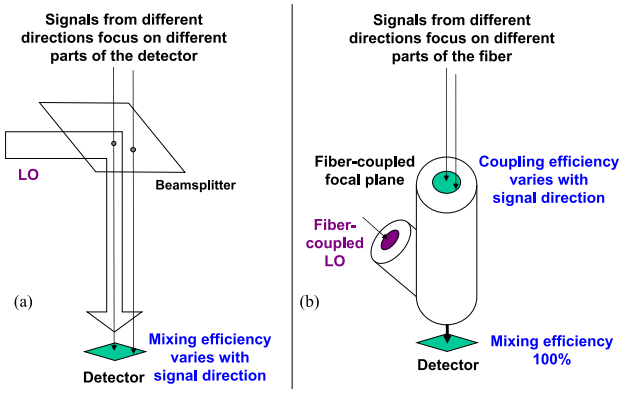

Fig. 7. (a) Spatially combining signal and optical LO with a beamsplitter. (b) Combining signal and optical LO into a single-mode fiber.

PHD collected below this minimum rate would make an image with azimuth ambiguities—a single pixel would contain features in the main lobe of multiple target points. Azimuth ambiguities are mitigated by using a repetition frequency sufficiently larger than the limit in (8), typically at least

$$f_{\text{pulse}} \geq \frac{4\omega R}{D}. \tag{9}$$

If the reflected signal of pulse N overlaps on the reflected signal of pulse $N+1$, then the PHD could have range ambiguities—a single range compressed image pixel could contain features of multiple range points. Range ambiguities, for a SAR/SAL looking at the ground, are mitigated by using an IPP that puts pulse-N sidelobes outside the antenna pattern (farther downrange) when pulse $N+1$ arrives. A SAL with main lobe larger than the target range extent, collecting PHD on a satellite with nothing behind it but empty space, should not have any range ambiguities.

The MNR quantifies the magnitude of ambiguities, near sidelobes, ISLR, sampling quantization, and any other effect which depends on signal strength.

SAL and SAR suffer from many signal losses in the path from coherent signal generation to detection and image production. The signal power of a SAR or SAL from coherent source to image is summarized in Fig. 6. There are signal losses in the transmitter path from source through the transmitter to free space, in the atmosphere due to scattering and absorption, in the receiver path from free space to detector, orientation of the sensor with respect to the LOS to the target, and noise-equivalent losses due to artifacts of digital processing. The target usually is larger than the SAR or SAL beam, so the beam does not have a uniform irradiance projected on the target; this increases the PHD noise level at the edges and corners of the image and is accounted for as LOS-dependent "corner loss" in some parts of the image including losses from azimuth compression. Atmospheric turbulence, even after correction with adaptive optics, causes spreading of the SAL transmitted beam with concomitant loss of signal on target (Strehl ratio < 1) and a reduction of focused received power onto the optical heterodyne detector (also Strehl ratio < 1); these unique optical signal losses are implicit in the transmitter and receiver efficiencies. Processing losses include the equivalent increase of noise in temporal frequency compression of the range pulses, as well as other noise-like effects in image formation processing. The effective source-to-image signal transmission fraction, combining all these losses, is L_C in the energy-aperture (3)

$$L_C = L_{xmt}\, L_{\text{atm}}^2 L_{\text{rcv}} \begin{Bmatrix} L_{\text{spot}}\,(\text{LOS}) \\ L_{\text{scan}}\,(\text{scan}) \end{Bmatrix} L_{\text{proc}} L_{\text{misc}}. \tag{10}$$

The two terms in (10) account for the corner and edge losses in spotlight and scan collection including LOS dependence of the heterodyne detector, pointing bias, and azimuth filtering over the spotlight or scan CPP.

Optical SAL/ISAL also is limited by detector quantum efficiency Q_e and by the efficiency of heterodyne detection η_{het}, which is always < 1 (and often $<<1$) [27]; we show this loss separately as $\eta_d = Q_e\, \eta_{\text{het}}$ in (3) because it is unique to SAL.

The SAL analog of "antenna pattern" is the heterodyne detector angular sensitivity. The finite size of the optical detector, and the need to spatially overlap the SOLO with the received signal, results in additional noise from real-aperture amplitude and phase fluctuations. There are two general ways to couple the optical LO and the received signal: a) spatially combine the SOLO and signal with a beamsplitter and propagate them both to the detector, or b) couple the SOLO and signal into a single-mode optical fiber and propagate that mode to the detector. These are illustrated in Fig. 7. The sensitivity of heterodyne efficiency to LOS in combining method (a) is shown in Fig. 8 (parameters just for illustration, not optimized). In method (b), the coupling efficiency of signal power into the single-mode fiber also is sensitive to LOS; after coupling into the fiber, both the SOLO and the signal are in the single mode of the fiber and overlap with 100% heterodyne efficiency. Whatever method is chosen, its LOS sensitivity must be considered in estimating heterodyne efficiency for (3).

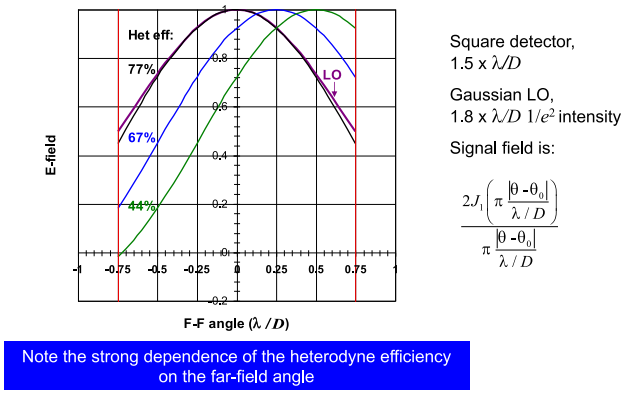

Fig. 8. Heterodyne efficiency of method (a) in Fig. 7 (parameters for detector size and LO shape not optimized). Heterodyne efficiency depends on the far-field (F-F) angle of the LOS to a point on the target.

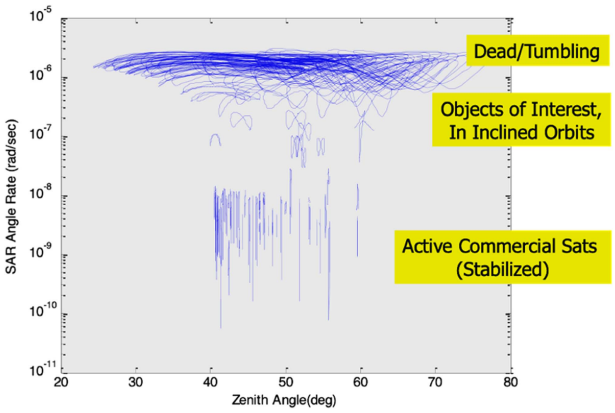

Fig. 9. Apparent rotation rate of various GEO objects over 24 h as would be seen from SOR on one day in 2007, if staring at Earth's center while under Keplerian motion. [Satellite data from the USSPACECOM satellite catalog.].

V. NATURAL SATELLITE MOTION

Keplerian orbital motion of a satellite around the Earth causes it to appear to rotate with respect to the ground everywhere on the Earth's surface except a ground point where the satellite is pointing (if it is pointing to someplace on the Earth's surface). Even satellites in geostationary orbit that are actively trying to remain at a fixed altitude over a specific point on the Earth's surface appear to rotate slowly. See Fig. 9, which shows the rotation rate of GEO objects due to Keplerian motion with respect to an observer at the Air Force Starfire Optical Range.

The apparent rotation rate, depending on the GEO satellite, can vary from nanoradian per second up to tens of microradian per second. The most interesting objects are in inclined orbits and appear to rotate at $\sim$1 μrad/s. Note that some objects move over a wide zenith angle; multiple images over diverse target aspects may be fused into a 3-D satellite model.

Fig. 10 is an example of the motion of a geostationary commsat, Echostar 6, which maintains its pointing toward Earth's center. Its rotation rate is very low, but not zero.

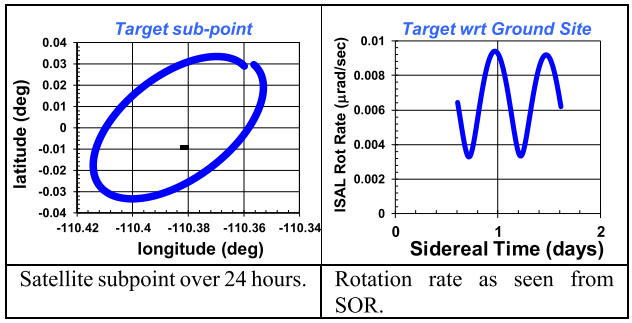

Fig. 10. Apparent rotation of echostar 6 GEOsat on day 121 of 2007.

The apparent rotation rate to an observer on the Earth's surface (or on a platform above the Earth) depends on many variables: the satellite element set, the Earth surface location it is pointing at, internal satellite motion, and the location and motion of the observer. In general, if the displacement of the ground site relative to the satellite is $\boldsymbol{R} = R_{\mathbf{obs}} - R_{\mathbf{sat}}$, the velocity of the satellite relative to the ground site is $\boldsymbol{V} = \boldsymbol{V}_{\rm obs} - V_{sat}$, and the satellite has a fixed orientation with respect to its velocity vector, then the angular velocity of the observer site around the satellite due to Keplerian motion is

$$\boldsymbol{\omega}_0 = \boldsymbol{R} \times \boldsymbol{V}/R^2 \,. \tag{11}$$

Note that the SAL image plane (slant plane) is the plane normal to the vector $\hat{\boldsymbol{n}} = \mathbf{R} \times \mathbf{V}/|\mathbf{R} \times \mathbf{V}|$. The rotation velocity should be calculated in a *body-fixed frame of the satellite*, the appropriate rotation rate for (3). If the satellite is rotating at speed $\boldsymbol{\omega}_{\mathbf{sat}}$ in the frame of calculation, then the apparent rotation rate of the observer around the satellite in a body-fixed frame is

$$\omega \;=\; |\boldsymbol{\omega}_0 - \hat{\boldsymbol{n}} \cdot |\, \boldsymbol{\omega}_{\rm sat} \cdot \hat{\boldsymbol{n}}|| \,. \tag{12}$$

If, for example, the satellite is in a circular orbit and rotating in an inertial frame to stare toward the Earth's center, then

$$\boldsymbol{\omega}_{\rm sat} = (V_{\rm sat}/R_s\,)\hat{\boldsymbol{q}} \tag{13}$$

where $\hat{\boldsymbol{q}}$ is the unit vector in the direction of orbital angular momentum in the inertial frame.

The rotation rate depends on many great satellite and sensor variables, too many to present rotation rate predictions for all interesting target/sensor pairings. However, we can calculate a simple example to illustrate the magnitude of Keplerian rotation. Fig. 11 shows the geometry of the example: the satellite is in a prograde circular orbit in the equatorial plane with semimajor axis R_s, the observer is on the equator viewing the satellite at zenith angle ζ, and the satellite is nadir-pointing to the center of the Earth. The rotation rate of the ISAL around the satellite in this simple example is

$$\omega \;=\; \frac{(V_{\rm sat} - V_{\rm obs})}{R_s}\,\frac{\sin\zeta}{\sin\varepsilon}\cos\left(\zeta - \varepsilon\right) - \frac{V_{\rm sat}}{R_s} \tag{14}$$

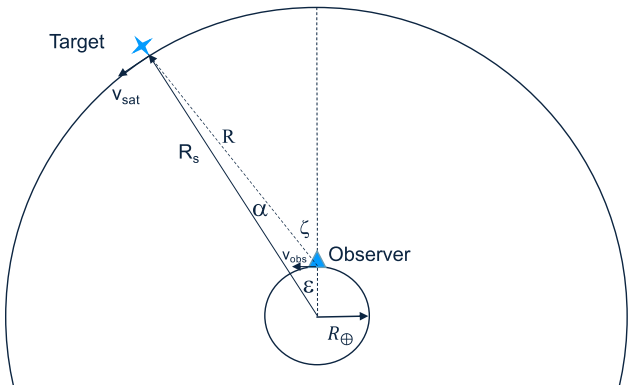

Fig. 11. Simple example for calculating satellite apparent rotation rate with respect to the ISAL. The satellite is in the equatorial plane, nadir pointing at Earth's center as it moves around Earth in its orbit with semimajor axis R_s and speed V_{sat}, and the observing ISAL is on the Equator of the rotating Earth with speed V_{obs}. The Doppler cone angle $\varphi = \frac{\pi}{2} + \alpha$.

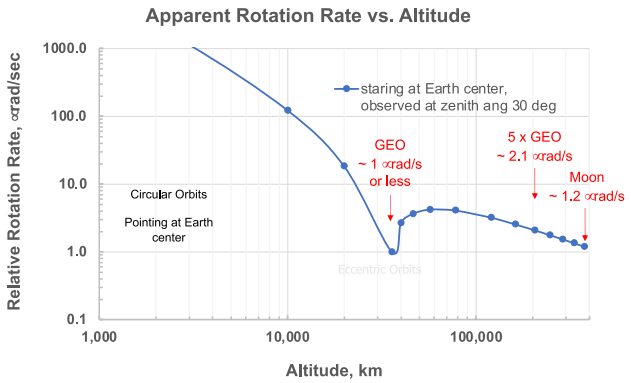

Fig. 12. Apparent rotation rate for the example of Fig. 11. Rate at the GEO altitude is set to = 1 μrad/s to include the "fast" rotating objects in Fig. 9.

where ε is the satellite Earth-center angle with respect to the observer

$$\varepsilon = \zeta - \sin^{-1}\left(\frac{R_\oplus}{R_s}\sin\zeta\right). \tag{15}$$

Fig. 12 shows ω calculated for this geometry observed at zenith angle $\zeta = 30°$ from a site on the equator. The rotation rate may be somewhat larger or smaller for other orbits, observer latitudes, and zenith angles. Later, we will use this rough estimate to predict approximately how much ladar power is needed for ISAL.

How much rotation do we need for ISAR or ISAL imaging with centimeter-class IPR? It depends on the frequency or wavelength of the SAR/ladar. Fig. 13 shows the rotation angle needed for X-band ISAR, W-band ISAR, and a 1 μm ISAL for targets in the geometry of Fig. 11, using (2) with $\kappa_a = 1$. RF ISAR needs rotations on the order of ~0.1–1 rad to get 1" IPR PHD, or needs multiple radar receivers spread out over that angle in a long baseline array. At the typical rotation rates of GEO and deeper space objects, RF ISAR at 1" azimuth IPR would require collecting for tens of thousands of seconds—not a practical endeavor. However,

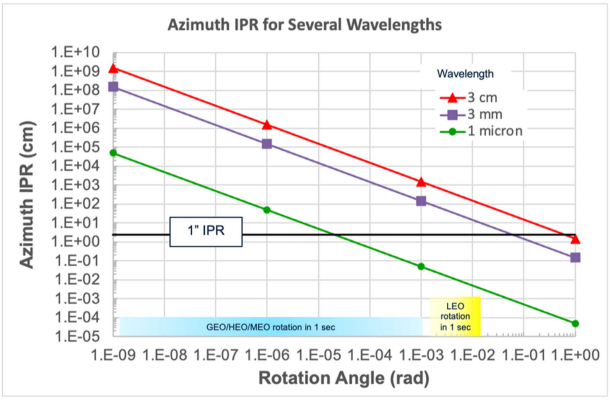

Fig. 13. Azimuth IPR as a function of rotation angle for ISARs of various wavelengths.

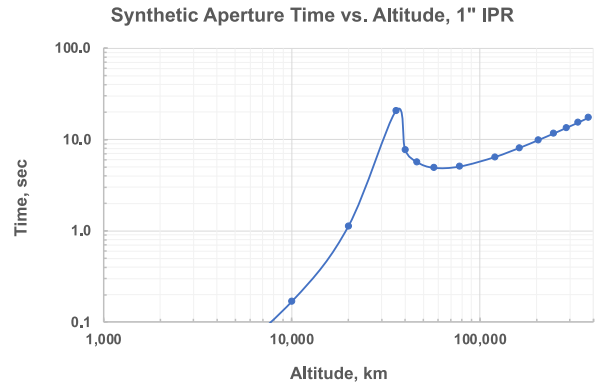

Fig. 14. Synthetic aperture time for a 1 μm ISAL to collect 1" IPR PHD in the geometry of Fig. 11.

a 1 μm ISAL would require a target rotation of only ~1–10 μrad to collect 1" IPR PHD, and this rotation is estimated to take 10 s or less. Fig. 14 shows the synthetic aperture time for a 1 μm wavelength ISAL to collect 1" IPR PHD in Fig. 11 example—depending on altitude, the CPP is only 0.1–20 s.

In addition to rigid-body rotation to point at Earth's center or at a fixed point on the ground, real satellites make many other motions. They may, for example, scan parts of the Earth's surface much faster, or slower, than assumed in Fig. 11. They may not move smoothly but instead may appear to jump from one orientation to another with a high instantaneous rotation rate. They may have articulated parts that rotate differently than the main satellite body. The motion of parts of the satellite may be intermittent instead of smooth; typical GEOsats, for example, have the solar panels move in a "jumpy" way about once per second to stay normal to the Sun. Intermittent motions and jumps may generate shaking or vibration in the whole satellite, and motion of a range-azimuth cell by only one wavelength of light, if not compensated, would destroy the coherence needed for azimuth compression. Typically, satellites are designed with natural mode frequencies <30 Hz, and the accelerations imparted by intermittent movement of large structures such as solar panels make only very small

and quickly damped displacements of other parts of the satellite [50].

Many of these motions can be discovered and compensated for in postprocessing [28]. Similar issues affect airborne ISAR imaging of ships at sea. Ships pitch, roll, and bend in unpredictable ways due to sea state, yet this motion can be compensated in processing the PHD, and airborne ISAR can make good images of ships. The ISAL aperture time may be shorter than the time between "jumps," so the jumps may have minimal effect the PHD. If the "jumps" occur at a steady rate then the satellite will vibrate at characteristic frequencies, and appropriate PHD processing can find the frequencies and compensate for the vibrations and for other repeatable satellite motions excited by the jumps.

We conclude that satellite Keplerian motion around the Earth is sufficient for high-resolution ISAL imaging; more complex motions of the satellite or parts of the satellite could generate a small-IPR image after appropriate motion compensation in signal processing.

VI. ISAL COHERENCE REQUIREMENTS

For ISAL, the ideal stable optical reference oscillator or SOLO has only "small" phase drifts over the round-trip time of a pulse. Intuitively the SOLO optical linewidth should be ~[round-trip time]$^{-1}$. This requirement can be refined by calculating the effect of SOLO phase shifts on impulse response sidelobes [29].

It is convenient for us to distinguish three frequency bands of the SOLO PSD, each making a distinctive image quality defect. 1) The "low" band has the frequencies $f \leq 1/2T_{\text{coh}}$, where T_{coh} is the time span of all the sampling pulses used to image one point on the target. The ideal resolution of a SAL of wavelength λ at range R and speed $V = \omega R$ normal to the line-of-sight is $\rho_{az0} = \lambda R/2VT_{\text{coh}}$. Low band error is quantified by the quadratic phase error on the PHD, which defocuses the signal in each pixel, i.e., increases the azimuth IPR 3 dB width. 2) The "mid" band has the frequencies $1/2T_{\text{coh}} \leq f \leq 2/T_{\text{coh}}$. Frequency errors in the midband generate sidelobes to the impulse response close to the main lobe (sidelobes larger than would result from error-free data, tapering, and processing), near the first or second sidelobes of the ideal impulse response. Midband error is quantified by the resultant peak sidelobe ratio (PSLR). 3) The "high" band has frequencies from $f = 2/T_{\text{coh}}$ up to the clutter cutoff frequency of the image. Frequency errors in the high band generate sidelobe growth at the third and higher sidelobes of the ideal impulse response. High band error is quantified by the integrated sidelobe ratio (ISLR) of all energy beyond the second sidelobe. The amount of PHD error allowed in each band depends on the form of the SOLO PSD and the IPR, PSLR, and ISLR allowed in the imagery. Since we use "coherent on receive" and the SOLO compares the transmitted pulse phase at time t to the received pulse phase at time $t + T_{RT}$, the PHD PSD is the SOLO PSD attenuated by the cancellation ratio cr

$$cr = 2\sin\left(\pi f T_{RT}\right). \tag{16}$$

We are interested in SOLO noise in the "mid" and "high" bands of frequencies f since SOLO noise in these bands increases sidelobes in range and azimuth. The analysis, which we will not reproduce here, says the SOLO linewidth can be somewhat larger than ~$[T_{RT}]^{-1}$ while still giving low sidelobes after compression. The result for the PHD PSD in both bands is

$$U_{high}\left(f\right) \leq 8\, PSLR\, f^2 T_{ap}. \tag{17}$$

A single frequency line of a stable octave-spanning optical clock can be Pound–Drever–Hall stabilized to a noise-equivalent linewidth $\delta f < 1$ Hz [30], [31], sufficient to SORO stability for an ISAL to image satellites as distant as the Moon.

An ISAL, even if it has adaptive optics perfectly correcting the high spatial frequency turbulence in the transmitter and receiver real apertures, is sensitive to another effect of atmospheric turbulence (which RF SAR is not sensitive to): atmospheric "piston." The atmospheric turbulence phase shift includes the piston phase, a shift of the atmospheric optical path length that is approximately uniform over the entire real aperture. The power spectral density of piston phase error due to Kolmogorov turbulence was first calculated in closed form in 2007 [32]. Piston changes occur whenever the outer scale of turbulence is larger than the real aperture, $l_0 > D$, and the synthetic aperture time is sufficient to move multiple outer scale turbulence cells through the real aperture $T_{\text{ap}} > l_0/V_{\text{wind}}$. Wavefront sensors measure the spatial and temporal variation of the phase of a point inside the aperture relative to other points but have no absolute optical phase reference to compare to, so consequently they neither measure the piston phase nor observe temporal changes in it. The changing piston phase adds a varying phase error to each PHD azimuth sample, illustrated in Fig. 3. Piston phase shifts may accumulate over the synthetic aperture time; models of Kolmogorov turbulence predict that the piston phase, depending on λ and D, may randomly walk by many radians over a few seconds [24]. If not corrected, random azimuth phase error at scales ρ between the real and synthetic apertures, $D < \rho < L$, would limit SAL resolution [25]. This phase error must be removed in postcollection PHD signal processing.

Finally, there is another atmospheric noise source in ISAL. Even after very good adaptive optics in the receiver real aperture, the optical field in the receiver pupil will have residual spatial variations in amplitude and phase. The optical field at the focal plane, location of the heterodyne detector or single-mode fiber coupler, is the Fourier transform of the pupil plane field. Ideally, we want to measure the phase of the center of this focused beam. But a real heterodyne detector, and a real single-mode fiber, has finite size, so we measure the weighted phase over this finite part of the focused beam. When this less-than-uniform optical beam is focused on the finite-sized heterodyne detector or finite-sized single-mode fiber, the spatial variations in the pupil convert into PHD noise. An accurate estimate of the noise considers the finite size of the detector. This is illustrated in Fig. 15. The focused field is the Fourier

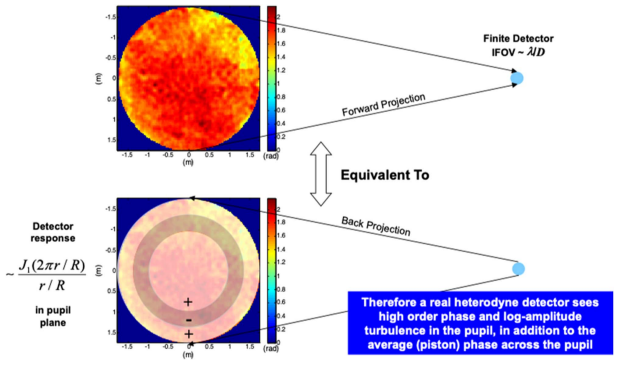

Fig. 15. Upper picture: Received signal spatial phase variation in the pupil after adaptive optical correction. Lower picture: The finite circular detector backprojects to a mask on the pupil plane with Airy function amplitude and alternating $0/\pi$ phase rings. Integration over the pupil shows how residual spatial noise enters the detected signal.

transform of the pupil field. By the Plancherel theorem, the focused field integrated over the finite detector is the same as the backprojection of the detector integrated over the pupil field. This backprojected detector is a spatially modulated function. A point detector (impossible in practice) would backproject to a constant over the pupil, while a finite circular detector backprojects to an Airy function [33]. The PHD noise due to pupil field spatial variations is the integral of the pupil field weighted by the Airy function. This noise, such as high-frequency LO noise, increases the sidelobes in range and azimuth; it is a unique optical source of multiplicative noise.

If the transmitter and receiver apertures have good adaptive optics producing a high Strehl ratio, then most of the ISAL-unique noises are small. Nevertheless, they must all be considered when estimating L_C and the power required by the energy-aperture theorem.

VII. LASER SOURCE POWER FOR DEEP-SPACE ISAL

Research on ISAL of GEOsats continued after the DARPA *LongView* program [34]. The Air Force Research Laboratory attempted ISAL satellite imaging of GEOsats in 2016–2018 in a program called GEO Multifunctional Aperture Synthesis Transceiver/Long-Range Imaging Ladar (LRIL) [35]. LRIL results are not publicly available, but undoubtedly were limited by laser source power. Laser power available at good beam quality in the mid-2010s was far less than is available today.

Today, we have HEL sources with excellent beam quality and coherence at peak powers up to and exceeding 300 kW, produced by the DoD HEL Scaling Initiative (HELSI) program [36]. We also have some very large aperture telescopes that could be used as ISAL transmitters and receivers. One could consider using, for example, the 3.6 m telescopes at MSSS or SOR, or for example, an 8.4 m telescope, such as the large binocular telescope (LBT) on Mt. Graham, AZ. What sort of ISAL could we make?

The performance of an ISAR or ISAL depends on great many design parameters. We choose some nominal ISAL design parameters to make preliminary estimates of ISAL performance. These do not represent a definitive ISAL design, and we do not claim these parameters are optimum for any particular ISAL metric or mission. Many of these design parameters are similar to what one would use in a LEO-satellite imaging ISAR or an airborne ground-imaging SAL. The key parameters are summarized in Table I.

TABLE I
Notional, Moderately Conservative, Design Parameters for a Deep Space Imaging ISAL

Parameter	Value	Units	Comment
Aperture Diameter D	0.72, 3.5 or 8.4	m	Transmitter and Receiver
Range IPR ρ_r	2.5 or 7.5	cm	Bandwidth = 8 GHz or 2.7 GHz
Azimuth IPR ρ_{az}	2.5 or 7.5	cm	
Taylor Weighting (sidelobe level and order)	(-35, 5)		Radar standard
Image CNR	> 7	dB	High contrast imagery
CNR Design Margin M	3	dB	Minimum radar standard
Wavelength λ	1.05	μm	
Beam Divergence FWHM at transmitter	1.15	x λ/D	VBQ $m^2 \sim 1.3$
Strehl Ratio of Atmospheric AO (1-way)	0.35		$\sim\lambda/8$, somewhat aggressive
Transmitter Duty Factor	Monostatic 45%		Bistatic 100%
Target Backscatter σ_0	-3.4	dB	Equivalent Lambertian reflectivity 46%
Round-Trip Losses wrt perfect propagation without free-space loss or backscatter loss	-10	dB	~90% power is lost in optical transport, atmospheric extinction, and signal processing
Detector Efficiency $\eta_d = Q_e * \eta_{het}$	0.75		GaAs or HgCdTe detector, fiber coupled to SOLO
Detector Noise Figure F	3	dB	Very good

We assume the depolarized backscatter is −1.9 dB and depolarization loss is −1.5 dB (only about 70% of it is in the same polarization as the incident laser light). If the average surface of the target is inclined ~45° to the incident beam, this corresponds to 46% average Lambertian reflectivity—a conservative assumption of a fairly dim and gray satellite target. We assume the receiver detects only one polarization of light, so we have put depolarization loss into σ_0.

A ladar illuminating satellites must point its beam ahead of the target to account for the finite speed of light. The point-ahead angle depends on the satellite orbit, the satellite location in that orbit, the ladar location on the rotating

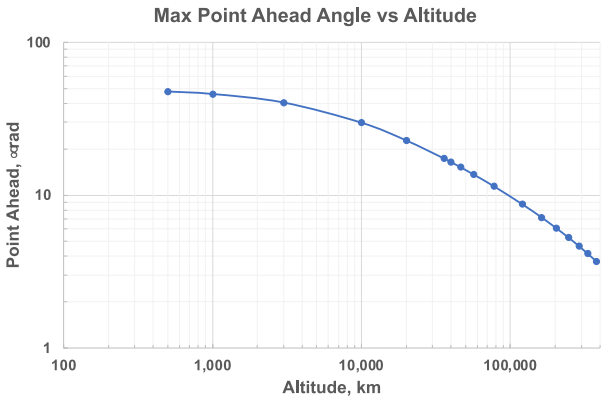

Fig. 16. Maximum point ahead angle for an observer at the Equator illuminating a satellite at zenith angle $\zeta = 0°$ in circular orbit in the equatorial plane.

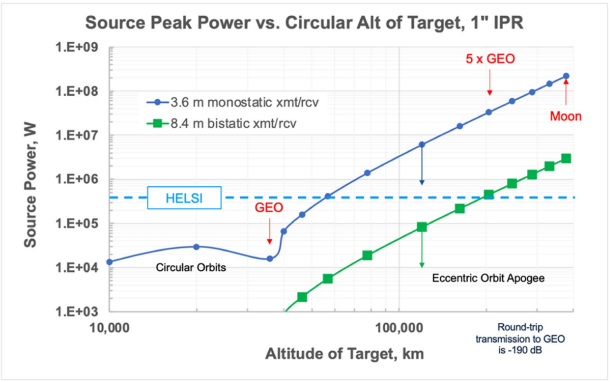

Fig. 17. Source laser power for ISAL with 1" range IPR, Table I design parameters, and Fig. 12 rotation rate. The monostatic system operates at a 45% duty factor, and the source power is the laser peak power. The bistatic system operates at 100% duty factor, and the source power is the laser CW power.

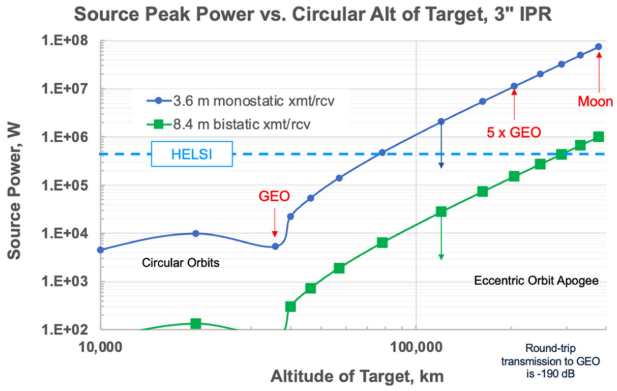

Fig. 18. Source laser power for ISAL with 3" range IPR, Table I design parameters, and Fig. 12 rotation rate. The monostatic system operates at a 45% duty factor, and the source power is the laser peak power. The bistatic system operates at 100% duty factor, and the source power is the laser CW power.

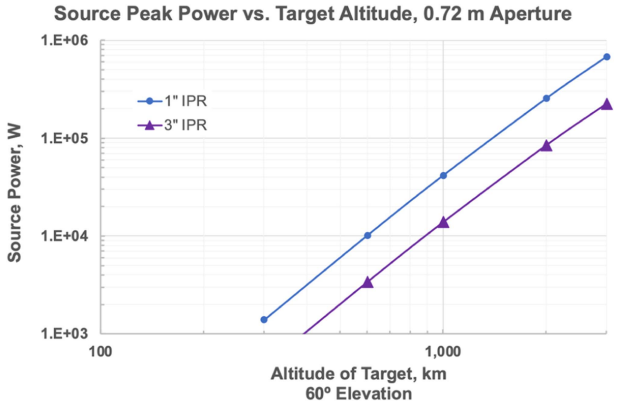

Fig. 19. Monostatic source peak power for ISAL imaging of LEO satellites. The source operates at a 45% duty factor, and the ISAL has Table I design parameters and Fig. 12 rotation rate. The targets are assumed to be at a 30° zenith angle, so the target range is slightly greater than the altitude.

Earth, and the aspect angle between the orbit and the ladar beam. The maximum point ahead angle of $2V/c$ occurs for a satellite passing through the observer's highest elevation angle. Fig. 16 shows the max point ahead for a ladar on the Equator and a satellite in a circular orbit passing through observer's zenith. For LEO targets, the max point ahead is < 50 μrad. It shrinks with altitude and becomes very small for deep space objects. For example, the point ahead angle to the Moon is less than 4 μrad.

Since Table I represents nominal ISAL parameters in the general design space, the power in these figures should be understood as representing the approximate power needed in this general design space, and not as definitive requirements of an optimized ISAL design.

We estimate the laser source power required for an ISAL to image satellites using the nominal design parameters of Table I, the target satellite Keplerian rotation rate of Fig. 12 circular orbits over the ISAL, and (3) from the SAR energy-aperture theorem. Results for 1" IPR in deep space are in Fig. 17; results for 3" IPR in deep space are in Fig. 18. Results for LEO satellites are in Fig. 19.

Our result is that an ISAL with laser source of peak power approximately 16 kW, with the notional ISAL parameters of Table I and a 3.6 m aperture with good adaptive optics (like the ones at MSSS or SOR), could image GEO satellites with CNR = 7 dB at IPR as small as ∼1", and a HELSI-class 300 kW laser in that same aperture could image satellites at nearly 2×GEO with CNR = 7 dB at IPR as small as ∼3". Our result is an ISAL with a HELSI-class laser source, bistatic 8.4 m apertures, and good adaptive optics (like the LBT on Mt. Graham, AZ) could image satellites in cis-lunar space at 6×GEO with CNR = 7 dB at IPR of approximately 3". Scaling the result in Fig. 17 with (6), the same HELSI-class ISAL with 8.4 m apertures could image the Lunar surface (the part we can see) with CNR = 7 dB at IPR of approximately 10". Results in Figs. 17–19 are calculated for circular orbits; eccentric orbits at apogee, such as for HEO satellites, could be imaged to those IPRs with less power or even smaller IPR with full power.

Note that there is very large signal attenuation in the round-trip from source to detector: round-trip signal power to GEO is approximately −190 dB less than the source power.

Our result also is that an ISAL with a laser source of peak power approximately 10–100 kW, with the ISAL

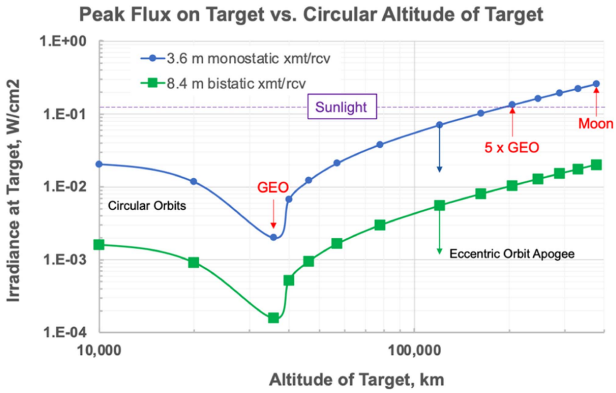

Fig. 20. Predicted peak flux on target for the ISALs of Fig. 17 with 1" range IPR.

parameters of Table I and a relatively small 0.72 m aperture with good adaptive optics, could image all LEO satellites with CNR = 7 dB at IPR of approximately 1–3". We assumed a small aperture for this system so that 1) it could be mobile (perhaps even in an aircraft platform) and operate from theaters of operation without large telescopes, and 2) the beam would be spread over a ∼1 m spot at range ∼1000 km, covering or easily scanning over the entire LEO target.

We stress again that these are preliminary results based on the nominal ISAL parameters of Table I and are not optimized for any specific imaging mission. They show the general class of performance a ground-based ISAL could achieve with today's HELs but should not be taken as definitive design requirements or performance predictions.

The power in Figs. 17–19 is calculated using the rotation rate in Fig. 12. This rotation rate is appropriate for satellites pointing at the Earth's center. At faster rotation rates, the ISAL would require correspondingly higher power or the CNR or resolution would be correspondingly lower.

A 1 μm wavelength laser is not eye-safe, and EO sensors have small but nonzero sensitivity to 1 μm light. A natural concern for a 1 μm ISAL is the possibility of satellite sensor damage. Fig. 20 shows the predicted peak flux on a satellite target for the large-aperture ISALs of Fig. 17.

A 1-μmISAL, despite using a non-eye-safe wavelength, might not present any danger to a satellite sensor, and the choice to use a 1-μm laser illuminator is a policy issue, not a technical one. Note that the ISAL in a 3.6 m aperture puts a flux on GEOsats ∼70× less than sunlight; the ISAL in bistatic 8.4 m apertures puts a flux on GEOsats ∼850× less than sunlight, and 6–250× less than sunlight throughout cislunar space out to the surface of the Moon. The flux on the sensor would be at or below the level of the Sun seen through strong sunglasses, and the synthetic aperture collection time would be short (typically < 10 s to GEO and beyond). The ISAL LEO imager of Fig. 19 may put a flux > sunlight on a LEO sat, but the synthetic aperture time of a LEOsat is only a few milliseconds. The possible ISAL damage to an unprotected EO sensor would depend on that sensor's instantaneous field-of-view (IFOV). A sensor would only get ISAL flux on its focal plane if the ISAL transmitter were inside the sensor field-of-view. Unprotected sensors looking in the vicinity of the ISAL may only be temporarily dazzled and not suffer irreversible damage.

Satellite operators could protect spacecraft from ladar damage similarly to how they protect from radar damage. All satellites are subject to ground-based radar tracking, and satellite operators take measures to protect their satellite RF systems against damage from high-peak-power radar pulses. Similarly, many satellites are routinely tracked by ground-based lasers for Earth geodesy research. Consequently, many Earth-looking satellite sensors have filters to protect them against common laser wavelengths. Satellite operators in the future could be warned that they point their sensor at the ISAL site at their own risk, just as they point unprotected RF apertures at radar tracking sites today at their own risk. Finally, research is underway to develop 2-μm lasers with high power comparable to the 1-μm HELs [37]. Equation (6) shows that ISAL performance is only indirectly sensitive to wavelength through the backscattering of satellite surfaces. So, if such 2 μm HELs become available, they would be an eye-safe and sensor-safe source for a ground-based ISAL with performance similar to Figs. 17–19.

VIII. SOME FEATURES OF ISAL FOR DEEP SPACE IMAGING

Throughout this article, we have analyzed a SAL/ISAL as a radar with carrier frequency ∼300 000 GHz. We are convinced that this is the correct approach. Analyses using standard concepts and tools of EO/IR sensors (either direct detection or coherent) or directed energy devices are likely to be misleading and overlook essential features of a SAL/ISAL.

An ISAL would be a "soda straw" sensor with a small IFOV equal to the transmitter main lobe width (∼the diffraction limit) and receiver diffraction limit. For example, the IFOV at 1 μm would be ∼0.3 μrad for a 3.6 m aperture system and ∼0.12 μrad for an 8.4 m aperture system. These would have IFOV of ∼12 m and ∼5 m at GEO, comparable to (or possibly smaller than) the size of some satellites in GEO. If the target satellite is larger than the IFOV of the ISAL transmitter or receiver aperture, then range and/or azimuth ambiguities may cause aliasing of parts of the satellite outside the IFOV into the image. This issue is not unique to ISAL imaging of satellites: an airborne SAR (RF radar) collecting PHD of the ground receives the reflected RF signal from an essentially infinite target >> RF antenna main lobe, so it is designed and operated to produce nonaliased imagery. A ground-based ISAL collecting PHD of satellites is less susceptible to aliasing because the reflecting target has a finite size in range and azimuth with nothing outside it to reflect signal energy back to the receiver. Range and azimuth ambiguities may be mitigated by the appropriate choice of laser pulse duration and repetition rate [see (9)] by increasing the IFOV to cover the entire target, or by using N detectors in the receiver covering N IFOVs and increasing the pulse repetition rate by factor N—mature mitigations developed for SAR.

ISAL pointing jitter would create amplitude and phase noise in the PHD. Consequently, a satellite imaging ISAL would need very stable pointing and tracking of the target and would need to suppress mechanical and atmospheric jitter to << 1 laser beamwidth.

The ISAL, with a small IFOV, would not be a wide area "search" or tracking sensor; it would need to be cued to its targets. It would characterize targets that have already been detected and tracked by other sensors. In principle, an ISAL could image a field-of-view larger than one IFOV, for example, by collecting PHD over multiple synthetic aperture dwells, scanning over several IFOVs, or using multiple detectors in the receiver. Expanding the image to multiple IFOVs would require longer synthetic imaging time, or higher source power and higher pulse repetition rate for multiple detectors to avoid azimuth ambiguities. The power estimates of Figs. 17–19 are the powers needed in a single IFOV.

The ISAL optical architecture must take point ahead into account (see Fig. 16). The ISAL needs a very high level of isolation between the transmit and received paths, paths which must differ in LOS by the small point ahead angle as magnified by the transmit/receive telescopes. For example, a GEO-transmitted pulse would be about 190 dB greater than the GEO-reflected return pulse. The transmitted and received pulses must be separated in space and/or time over the small point ahead angle so that neither the transmitted pulse nor its atmospheric backscatter eclipses the received pulse. The clever optomechanical design could do this for a monostatic system (same aperture for transmitter and receiver) with temporal and spatial multiplexing to separate the beams at low or moderate power, and consequently could operate at a duty factor $< 50\%$ with temporal multiplexing such as a SAR. Dead time between transmit and receive in a monostatic system would need to include the time for atmospheric backscattering. At sufficiently high power, the spatial and temporal multiplexing may not be feasible in a single aperture. A very high power transmitter may need a bistatic architecture (separate apertures for transmitter and receiver). A bistatic system could operate at 100% duty factor if the receiver fields-of-view were sufficiently narrow to exclude atmospheric backscattering of the transmitted beam into the receiver.

PHD with pulse-to-pulse unknown phase error cannot focus energy into the image pixels. In Section V, we noted that ground-based ISAL PHD would contain atmospheric piston phase errors if $l_0 > D$ and $T_{\text{ap}} > l_0/V_{\text{wind}}$. A ground-based ISAL imaging GEO or above would need 1–10 s for a synthetic aperture, so it probably would drift through several different piston phases during T_{ap}. A ground-based ISAL imaging LEO would have a very short aperture time and may not be subject to piston drift in one T_{ap}. An airborne ISAL might fly through several (or many) different piston phases in one T_{ap} depending on its platform speed. SAL image formation processing would need to compensate for large random piston errors and various possible motion errors, including high relative speed between sensor and target. Many different signal processing approaches have been proposed [38], [51].

In the DARPA *LongView* program, prime contractor Northrop Grumman developed algorithms and PHD processing software to recognize piston phase drift and autofocus the PHD with piston [39]. RF SAR routinely needs autofocus processing to remove phase error from unknown SAR platform motion or target motion. The RF community has a suite of algorithms for autofocus, including entropy minimization and phase gradient autofocus. Most of these algorithms work best when there are some high-CNR target features that can be tracked in the PHD from pulse to pulse. Many RF algorithms tested in *LongView* did not work well for ISAL because satellite targets may have no easily trackable features and the PHD may have nonuniformly distributed random phase errors. Sharma [40] developed the iterative contrast enhancement (ICE) algorithm for ISAL autofocus of satellite PHD. These algorithms were applied to simulated PHD of modeled satellite targets with large random large piston errors over T_{ap} (many 100s of radians of error over ~100 s imaging windows). ICE is distinct from other proposed algorithms for ISAL imaging of satellites which deal only with smooth and predictable relative motion of a space-based ISAL but do not correct the large random and fluctuating atmospheric phase errors anticipated in a ground-based ISAL [49]. *LongView* successfully autofocused the PHD into small-IPR images. One of the key insights enabling autofocus without any trackable features is that many pixels in a focused satellite image should be empty (have no energy). The only pixels with energy should be on the target because nothing else reflects signal energy back to the receiver. Since the ISAL beam would be (or could be made) larger than the target satellite, the correctly focused PHD image should have more energy-empty pixels than energy-containing pixels. This constraint provides an overdetermined system of equations that we can solve for the piston phase errors. ICE worked very well to focus ISAL PHD, at wavelengths as short as 1 μm, with very large random piston error over the synthetic aperture.

The ISAL, being a coherent imager, would have laser speckle in its images. A single-look image of a flat-brightness target would have an average variation in pixel energy equal to the average pixel energy, so its SNR = 1. The ISAL could produce higher SNR by averaging several independent images. RF SAR images have the same fluctuation in pixel energy; the radar community refers to it as Swerling type-2 fluctuation [41].

IX. SUMMARY AND CONCLUSION

Based on the analysis presented here, we conclude that ground-based ISAL, using current HEL sources and current large telescope apertures with good adaptive optics, could image satellites at very high resolution (IPR of a few centimeters) in orbits from LEO out to the Moon and beyond. The ISAL could be cued by other deep space tracking sensor systems. Such imagery could be of great value for the

characterization of deep space objects. Although the ISAL would not be a wide-area search sensor, it also could search over small areas around critical space assets looking for and characterizing potential threats that come within the asset's keep-out zone. The ISAL could characterize the so-called "inspector" satellites doing rendezvous-and-proximity operations near our space assets.

A space-based SAL imager might also be useful for deep space object characterization [42]. A SAL on an "inspector" satellite in GEO or cis-Lunar space could collect high-resolution images of deep space targets at a longer range than a similar-sized passive imager, and the PHD would contain much more information than a passive image. A SAL on any platform, however, would be a complex sensor. It would be prudent to first demonstrate ISAL of satellites from the ground and work out all its issues and challenges, before trying to put ISAL on a satellite in deep space. Also, a SAL would generate a large amount of PHD, and image generation may require sophisticated processing to remove motion artifacts [51]. A ground-based ISAL could develop and test the phase history processing algorithms before trying to run them onboard a satellite.

Finally, the high-resolution imaging capability of an ISAL with power < 100 kW and a 0.72 m aperture, as shown in Fig. 19, could provide an interesting midcourse discrimination sensor for missile defense. The ISAL imagery could help recognize real targets among decoys. It potentially could be forward deployed on an airborne platform.

REFERENCES

[1] T. Hitchens, "'Critically important:' New White House strategy for cislunar research echoes Space Force," *Breaking Defense*, Nov. 17, 2022.

[2] R. Mola, "How things work: Space fence," *Smithsonian Magazine*, Feb. 2016.

[3] "Whats up there, where is it, and what's it dong? The U.S. Space surveillance network," Nat. Security Archive, George Washington Univ., Washington, DC, USA, Mar. 13, 2023.

[4] M. Czerwinski and J. Usoff, "Development of the haystack ultrawideband satellite imaging radar," *Lincoln Lab. J.*, vol. 21, pp. 28–44, Jan. 2014.

[5] T. Payne, "Space object characterization," NATO Rep. STO-EN-SCI-292, 2016.

[6] A. Abuter et al., "First light for GRAVITY: Phase referencing optical interferometry for the very large Telescope interferometer," *Astron. Astrophys.*, vol. 602, 2017, Art. no. A94.

[7] A. Hindsley et al., "Navy prototype optical interferometer observations of geosynchronous satellites," *Appl. Opt.*, vol. 50, pp. 2692–2698, 2011.

[8] S. Hensley et al., "Radar generates high-resolution topographic map of the Moon," *SPIE Newsroom*, Jun. 2008.

[9] "NASA's deep space network antenna captures radar images of Asteroid 1998 QE2 and its Moon as it past [sic] Earth," *Clarksville Online*, 7 Jun. 2013.

[10] "Holiday asteroid imaged with NASA radar," Dec. 21, 2018. [Online]. Available: https://www.nasa.gov/sites/default/files/thumbnails/image/pia22970-home.jpg

[11] D. Mensa, *High Resolution Radar Imaging*. Dedham, MA, USA: Artech House, 1981, ch. 3.

[12] F. Zernike, "Die Wahrscheinliche Schwingungsverteilung in Einer von Einer Lichtquelle Direkt Oder Mittels Einer Linse Beleuchteten Ebene," *Physica*, vol. 5, 1934, Art. no. 201; *Proc. Phys. Soc* ***61***(158) (1948).

[13] C. Jakowatz Jr., D. Wahl, P. Eichel, D. Ghiglia, and P. Thompson, *Spotlight-Mode Synthetic Aperture Radar: A Signal Processing Approach*. Norwell, MA, USA: Kluwer, 1996, ch. 2.

[14] D. Wetzel, "Digital methods for cohere-on-receive radar applications," Ph.D. dissertation, Engineering, Univ. Dayton, Dayton, OH, USA, Aug. 2018 (and references therein).

[15] T. Green, Jr., S. Marcus, and B. Colella, "Synthetic-aperture-radar imaging with a solid-state laser," *Appl. Opt.*, vol. 34, no. 30, pp. 6941–6949, 1996.

[16] M. Bashkansky, R. L. Lucke, E. Funk, L. J. Rickard, and J. Reintjes, "Two-dimensional synthetic aperture imaging in the optical domain," *Opt. Lett.*, vol. 27, no. 22, pp. 1983–1985, 2002.

[17] S. Beck et al., "Synthetic-aperture imaging laser radar: Laboratory demonstration and signal processing," *Appl. Opt.*, vol. 44, no. 35, pp. 7621–7629, 2005.

[18] Battlespace, London: Battlespace Publications, Aug. 14, 2006. [Online]. Available: https://battle-updates.com/update

[19] J. Ricklin, B. Schumm, M. Dierking, P. Tomlinson, and S. Fuhrer, "Synthetic aperture ladar for tactical imaging (SALTI)," AFRL-RY-WP-TP-2010-1063 briefing, Jul. 2007.

[20] J. Curlander and R. McDonough, *Synthetic Aperture Radar: Syst. and Signal Process.*. New York, NY, USA: Wiley, 1991, ch. 10.

[21] Military & Aerospace Electronics, Nashua, NH: Endeavor Business Media LLC, Dec. 7, 2006. [Online]. Available: https://www.militaryaerospace.com

[22] J. W. Goodman, "Synthetic-aperture optics," in *Progress in Optics Vol. VIII*. E. Wolf Ed., Amsterdam, The Netherlands: North-Holland, 1970, pp. 1–50.

[23] N. Vandenberg, "Derivation of the $\sigma_{\rm n}$ equation," ERIM memorandum DSAD-95-142A, Nov. 20, 1995.

[24] T. J. Karr, "Generalized energy-aperture product limit for Multibeam, spotlight and bistatic SAR," LLNL technical report UCRL-ID-123065, Dec. 21, 1995.

[25] R. Lucke and L. Rickard, "Photon-limited synthetic-aperture imaging for planet surface studies," *Appl. Opt.*, vol. 41, no. 24, pp. 5084–5095, 2002.

[26] T. J. Karr, "Resolution of synthetic-aperture imaging through turbulence," *JOSA A*, vol. 20, no. 6, pp. 1067–1083, 2003.

[27] R. H. Kingston, *Detection of Optical and Infrared Radiation*. Berlin, Germany: Springer-Verlag, 1978, chapter 3.

[28] W. Carrara, R. Goodman, and R. Majewski, *Spotlight Synthetic Aperture Radar Signal Processing Algorithms*. Boston, MA, USA: Artech House, 1995, ch. 6, 9.

[29] T. J. Karr, "Phase and frequency stability for synthetic aperture LADAR," in *Proc. SPIE Opt. Eng. Appl. Conf.*, vol. 6712-01, 2007.

[30] L. Hollberg et al., "Optical frequency/wavelength references," *J. Phys. B, Atomic, Mol. Opt.*, vol. 38, pp. S469–S495, 2005.

[31] T. M. Fortier et al., "Generation of ultrastable microwaves via optical frequency division," *Nature Photon.*, vol. 5, pp. 425–429, 2011.

[32] T. J. Karr, "Atmospheric phase error in coherent laser radar," *IEEE Trans. Antennas Propag.*, vol. 55, no. 4, pp. 1122–1133, Apr. 2007.

[33] *Max Born and Emil Wolfe, Principles of Optics*, 3rd (revised) ed. Oxford, U.K.: Pergamon Press, 1964, p. 396.

[34] C. J. Pellizzari, C. L. Matxon, and R. Gudimetla, "Inverse synthetic aperture LADAR for geosynchronous space objects—Signal-to-noise analysis," in *Proc. Adv. Maui Opt. Space Surveill. Technol. Conf.*, 2011.

[35] "GEOMAST request for information," Solicitation #FA8650-13-C_1525_GEOMAST_RFI, posted Nov. 26, 2018.

[36] "Lockheed Martin delivers its highest powered laser to date to U.S. Department of Defense," Loc kheed Martin news release, Sep. 15, 2022.

[37] "2-micron wavelength kilowatt class high energy laser/amplifier," DoD Contract N68335-20-C-0712, 2020.

[38] C. J. Pellizzari et al., "Synthetic aperture ladar: A model-based approach," *IEEE Trans. Comput. Imag.*, vol. 3, no. 4, pp. 901–916, Dec. 2017.

[39] S. Strauch, S. Wright, and S. Stevens, "LongView Phase-1 report part A," Contract FA856 0-07-C-7701, Apr. 8, 2008.

[40] R. Sharma, "Iterative contrast enhancement based SAR auto-focus algorithm," extended summary for the *LongView* program, internal Northrop Grumman publication, 2006.
[41] P. Swerling, "Probability of detection for fluctuating targets," The RAND Corp. ASTIA Doc. AD 80638, Mar. 17, 1954.
[42] V. Gamiz et al., "Active space-space synthetic aperture imaging LADAR (ASSAIL)," private communication, Jan. 26, 2021.
[43] D. Fried, "Optical heterodyne detection of an atmospherically distorted signal wave front," *Proc. IEEE*, vol. 55, no. 1, pp. 57–77, Jan. 1967.
[44] C. Clark, "IARPA, Amon-Hen & Aladdin: Next Gen Intel," breaking defense, Jun. 4, 2017.
[45] G. Overton, "IARPA Amon-Hen program seeks interferometer to image GEO satellites," Laser Focus World 9, Nov. 2017.
[46] S. R. Restaino et al., "Naval Prototype Optical Interferometer (NPOI) upgrade with light-weight telescopes and AO: A status update," in *Proc. AMOS Conf.*, 2006.
[47] S. R. Restaino et al., "Using optical interferometry for GEO satellites imaging: An update," in *Proc. SPIE*, vol. 9836, 2016, Art. no. 983603.
[48] F. T. Armstrong et al., "Observations of a geosynchronous satellite with optical interferometry," in *Proc. Adv. Maui Opt. Space Surveill. Technol. Conf.*, 2008, Paper 78180L.
[49] H. R. Schmitt et al., "Analysis of Galileo style geostationary satellite imaging: Image reconstruction," in *Proc. Adv. Maui Opt. Space Surveill. Technol. Conf.*, 2012.
[50] H. Yin et al., "Spaceborne ISAL imaging algorithm for high-speed moving targets," *IEEE J. Sel. Topics Appl. Earth Observ. Remote Sens.*, vol. 16, pp. 7486–7496, 2023.
[51] P. R. K. Chetty, *Satellite Technology and Its Applications*, 2nd ed. Blue Ridge Summit, PA, USA: McGraw-Hill, 1991, p. 76ff.
[52] X. Tong et al., "Refocusing of moving ships in Squint SAR images based on spectrum orthogonlization," *Remote Sens.*, vol. 13, no. 14, 2021, Art. no. 2807.
[53] W. L. Wolfe and G. J. Zissis, Eds., *The Infrared Handbook*, revised ed. Ann Arbor, MI, USA: ERIM, 1985, ch 3–5.

Thomas J. Karr (Life Member, IEEE) received the A.B. degree (*cum laude*) in physics from Princeton University, Princeton, NJ, USA, in 1971, and the Ph.D. degree in physics from the University of Maryland, College Park, MD, USA, in 1976.

He was with DARPA as a Program Manager during 2012–2018 and with the Office of the Undersecretary of Defense for Research and Engineering as the first Principal Director for Directed Energy during 2018–2020. He also served as the Director of Innovative System Solutions with Raytheon, the Director of EO/IR Technology with Northrop Grumman, an Executive Director of the Ellipso Satellite Telephone System, and a Senior Scientist and Program Leader with Lawrence Livermore National Laboratory. He is currently the MITRE Corporation Chief Scientist of Sensing and Directed Energy, and an advisor to the Assistant Secretary of Defense for Critical Technologies, the Defense Science Board, and the Air Force Scientific Advisory Board. He was a Fellow of the University of Maryland Center for Theoretical Physics during 1972–1974, and the Joliot-Curie Fellow of the Commissariat a l'Énergie Atomique of France during 1977–1978. His research interests include active and passive sensing of RF, EO/IR, X-ray and gamma radiation, imaging of the Earth from space and space from the Earth, space domain awareness, ground- and space-based astronomy, quantum sensors, optical propagation, nonlinear optics, photonic signal processing, optical clocks, pulsed laser–matter interactions, group theory and symmetries in physics, and quantum paradoxes. He is a Fellow of Optica, SPIE, and MSS.